


Spin mixing conductance and spin magnetoresistance of the iridate/manganite interfaceG. A. Ovsyannikov^{1,*}, K. Y. Constantinian¹, V. A. Shmakov¹, A. L. Klimov^{1,2}, E. A. Kalachev², A. V. Shadrin^{1,3}, N. V. Andreev⁴, F. O. Milovich⁴, A. P. Orlov¹ and P. V. Lega¹¹*Kotel'nikov Institute of Radio Engineering and Electronics, Russian Academy of Sciences, Moscow 125009, Mokhovaya 11–7, Russia*²*Russian University of Technology–MIREA, Moscow 119454, Vernadsky Av. 78, Russia*³*Moscow Institute of Physics and Technology (National Research University), Dolgoprudny 141701, Moscow region, Russia*⁴*National Research Technological University - MISIS, Moscow 119049, Leninsky Avenue 4, Russia* (Received 7 September 2022; revised 31 January 2023; accepted 24 March 2023; published 13 April 2023)

SrIrO₃/La_{0.7}Sr_{0.3}MnO₃ heterostructure including contact of 3d–5d materials with strong spin-orbit interaction in SrIrO₃ was fabricated by rf magnetron sputtering at high temperature. The epitaxial growth of the thin films in heterostructure by a cube-on-cube mechanism was confirmed by x-ray diffraction and transmission electron microscopy analysis. We present results of experimental studies of spin current and spin mixing conductance of the heterostructures measured under spin pumping at ferromagnetic resonance in wide-frequency band 2–20 GHz. Taking into account the contribution of anisotropic magnetoresistance the spin current was estimated as 1/3 of the total response. We show that both real and imaginary parts of spin mixing conductance are valuable for heterostructures with spin-orbit interaction in SrIrO₃. The spin Hall magnetoresistance of the heterostructure was evaluated from angular dependencies of either longitudinal or transverse magnetoresistance measured in planar Hall configuration. The influence of anisotropic magnetoresistance of La_{0.7}Sr_{0.3}MnO₃ film was taken into account as well. The spin Hall angle estimated from measurements of transverse magnetoresistance was found much higher than that obtained for interfaces with often-used spin-orbit interaction material like platinum.

DOI: [10.1103/PhysRevB.107.144419](https://doi.org/10.1103/PhysRevB.107.144419)**I. INTRODUCTION**

Using electron spins instead of electron charges opens up new opportunities in microelectronics, especially for reduction of heat dissipation in submicrometer-sized elements. The magnetization precession forced by microwaves at ferromagnetic resonance (FMR) generates pure (without electron charge transfer) spin current at the interface of metal/ferromagnet. Spin current can be converted to the charge current by means by inverse spin Hall effect (ISHE) [1–8]. This requires a completely different approach compared to charge-transfer electronics. A challenging task is the enhancement of efficiency of spin to charge conversion. Both the spin Hall effect (SHE) and ISHE lead to a change of magnetoresistance in a metal/ferromagnet (N/F) heterostructure depending on the direction of magnetization, called spin Hall magnetoresistance (SMR) [9–12], adopted as an effective tool for probing the spin Hall angle and spin-diffusion length.

The most common method for spin current generation is the use of spin pumping in the presence of FMR at the N/F interface. Indeed, under FMR a precessing magnetization in a ferromagnetic generates spin current via spin pumping and then converts at the interface with an adjacent normal layer to a dc voltage by ISHE. The amplitude of spin current depends on precessing magnetization and spin mixing conductance characterized by its real and imaginary parts. The efficiency of conversion of spin current to the charge current is characterized by the spin Hall angle θ_{SH} , which could be evaluated

as the ratio of the spin Hall magnetoresistance and the electroresistance of the N metal by means of magnetotransport measurements [13–15].

Studies on spin pumping and induced by ISHE the dc voltages in a F/N heterostructure were first carried out with the platinum (Pt) as a N metal in combination with the permalloy (NiFe-Py) as the F metal [4,16,17], and also using N metal contacting to the insulating ferromagnetic yttrium iron garnet [18–20]. At the same time a spin-orbit interaction (SOI) plays rather a decisive role and a variety of metals with strong SOI have been used in combination with the ferromagnetic materials [21,22].

Functional oxides, displaying intriguing interplay between charge, spin, orbital, and lattice degrees of freedom, offer a rich platform for both fundamental and application-oriented research. The physical properties of the oxide expanded from high-temperature superconductivity in cuprates, colossal magnetoresistance in doped manganites [23], and exotic band-structure effects in perovskite iridates [24]. Moreover, the sensitivity of complex oxides to epitaxial strain [25] which influences the interface chemistry and crystal orientation provides opportunities for tuning the electronic and magnetic structure, leading also to SOI effects. In particular, 5d transition-metal oxides (TMO) with strong SOI and electron-electron correlation pushed on studies of nontrivial quantum phases [26–28], magnetic anisotropy control [29], intrinsic charge-spin interconversion, and nonlocal spin current manipulation [30–33].

The studies of the charge-to-spin interconversion in structures with the promising SrIrO₃ 5d TMO [24] and the adjacent ferromagnetic have been carried out. A metallic

*gena@hitech.cplire.ru

polycrystalline compound deposited *ex situ* on SrIrO₃ such as SrIrO₃/Py [30,31], or SrIrO₃/Co_{1-x}Tb_x [32] structures are used. It was demonstrated that a large intrinsic spin Hall conductivity in SrIrO₃ arises due to SOI, producing Berry phase curvature on Fermi surface in electronic band structure [30,31]. The defining parameters which quantify the efficiency of spin-to-charge current conversion are as follows: the spin-diffusion length in the N metal (λ_{sd}), the spin Hall angle (θ_{SH}), and the spin mixing conductance ($g^{\uparrow\downarrow}$), which is determined by the scattering matrix for electrons at the N/F interface and characterizes the transparency of spin angular momentum transfer [6,34]. The evaluation of the above-mentioned parameters constitutes a delicate problem and it is the main task of our work. The relation between spin current generated by ferromagnetic resonance and the charge current characterized by spin Hall angle θ_{SH} was around 0.3 in structures [30–32] with the SrIrO₃ capping. For comparison, a structure of metallic Pt with Py had $\theta_{SH} < 0.1$ [5,9,16].

Recently it was shown that atomically perfect epitaxial interface of all oxide ferromagnetics and well-conducting (as a normal metal) material with SOI could be realized for manganite La_{0.7}Sr_{0.3}MnO₃ and the strontium iridate SrIrO₃ heterostructure grown by pulsed-laser deposition either on (LaAlO₃)_{0.3}(Sr₂AlTaO₆)_{0.7} (LSAT) or NdGaO₃ or SrTiO₃ substrates [35–37], as well by magnetron sputtering on NdGaO₃ [38]. An increase of Hilbert damping in FMR spectrum of SrIrO₃/La_{0.7}Sr_{0.3}MnO₃ heterostructure due to spin pumping was demonstrated [35,36,38] along with the estimations of real part of spin mixing conductance $\text{Re}g^{\uparrow\downarrow}$. However, the influence of imaginary component of $g^{\uparrow\downarrow}$ was not accounted [35,36,38]. The first experimental observations of spin current response from SrIrO₃/La_{0.7}Sr_{0.3}MnO₃ heterostructures was described by the sum of two contributions due to the spin current through the interface and the anisotropic magnetoresistance in La_{0.7}Sr_{0.3}MnO₃ [35,38,39].

The paper is organized as follows: Besides the Introduction in Sec. I, results of fabrication and structural study of SrIrO₃/La_{0.7}Sr_{0.3}MnO₃ heterostructures are given in Sec. II with the details on the samples characterization and experimental setup. In Sec. III we discuss the experimental data on the voltage caused by charge current in spin pumping regime obtained for La_{0.7}Sr_{0.3}MnO₃ film and SrIrO₃/La_{0.7}Sr_{0.3}MnO₃ heterostructure. Influence of the voltage response induced by anisotropic magnetoresistance was analyzed. The real and imaginary parts of spin mixing conductance of the heterostructure were determined from the frequency dependences of FMR spectra. Extremely high imaginary parts of spin mixing conductance were obtained. In Sec. IV we discuss results of the magnetoresistance measurements of both a La_{0.7}Sr_{0.3}MnO₃ film, and the SrIrO₃/La_{0.7}Sr_{0.3}MnO₃ heterostructures. The spin Hall angle was determined from the angular dependences of longitudinal and transverse magnetoresistance. An influence of anisotropic magnetoresistance on the SMR was observed. Conclusions are given in Sec. V.

II. MANGANITE/IRIDATE HETEROSTRUCTURES

Thin epitaxial films of strontium iridate SrIrO₃ (SIO) and manganite La_{0.7}Sr_{0.3}MnO₃ (LSMO) with thicknesses of 10

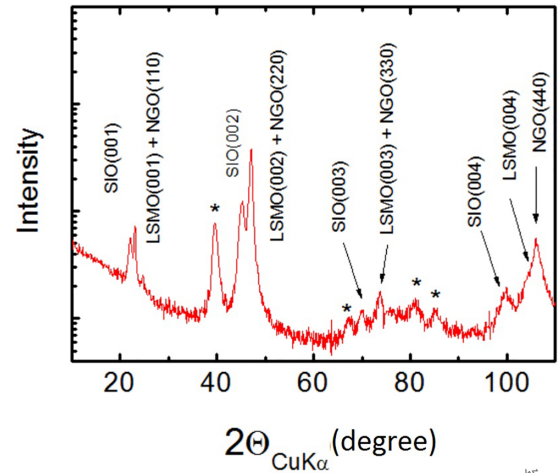


FIG. 1. XRD Bragg reflections for Pt/SIO/LSMO/NGO heterostructure. Reflections from the Pt are marked by an asterisk.

and 30 nm, correspondingly, were grown on single-crystal substrates (110)NdGaO₃ (NGO) by magnetron rf sputtering at substrate temperatures of 770–800 °C in Ar and O₂ gas mixture at the total pressure of 0.3 mbar [38,39].

Three types of heterostructures were prepared: (i) Pt/SIO/LSMO/NGO for x-ray (XRD) and transmission electron microscope (TEM) studies, using sample patterning by focused ion-beam (FIB) etching. Platinum protecting layer was deposited for technological reasons by magnetron sputtering and FIB technique before fabrication cross-section slice; (ii) strip-shape SIO/LSMO/NGO and LSMO/NGO heterostructures were used for ferromagnetic resonance (FMR) measurements; and (iii) SIO/LSMO/NGO, LSMO/NGO, and SIO/NGO heterostructures fabricated in planar Hall effect configuration for spin Hall magnetoresistance measurements.

The crystal structure of Pt/SIO/LSMO heterostructures has been studied by XRD analysis and TEM [38]. The crystal lattice of SIO and LSMO could be described as a distorted pseudocube with lattice parameters $a_{\text{SIO}} = 0.396$ nm and $a_{\text{LSMO}} = 0.389$ nm, respectively, as the (110)NGO plane could be considered as pseudocube with parameter $a_{\text{NGO}} = 0.386$ nm, with the difference of legs 0.12% that induces magnetic anisotropy [38]. Note, previously we have investigated also the inverted bilayer structures LSMO/SIO/NGO, as well as the Pt/LSMO/NGO in Ref. [38]. In all cases the LSMO and SIO films were grown epitaxially, while Pt was polycrystalline with the lattice parameter 0.392 nm.

Figure 1 shows XRD Bragg diffractogram of Pt/SIO/LSMO heterostructure. Multiple reflections from plane (001) of SIO film and reflections from (110)NdGaO₃ substrate, coinciding with the reflections from the plane (001) of LSMO, as well as the reflections from Pt film are seen. A thick Pt film was deposited only for type (i) heterostructures to prevent changing of the oxygen content in oxide film under the FIB etching. The XRD data in Fig. 1 and results of experiment in Ref. [38] allow to conclude that the growth of heterostructure is performed by the “cube-on-cube” mechanism with the following ratio: (001)SIO||[(001)LSMO]||[(110)NGO] and [100]SIO||[100]LSMO||[[001]NGO] [38].

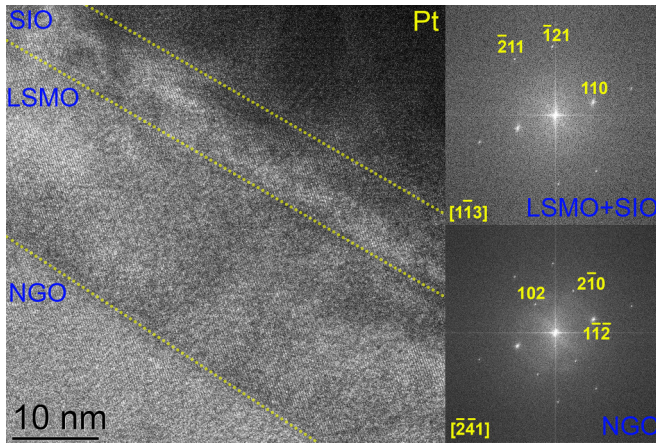


FIG. 2. TEM image of a cross section of Pt/SIO/LSMO/NGO heterostructure covered with a thick layer of Pt playing the charge-streaming cladding role. Electron diffraction from the NGO substrate regions and LSMO/SIO films are shown on the right. The yellow lines are drawn using electron diffraction data, image contrast, and EDX. A detailed analysis of EDX data gives transition layer 2–3 nm determined mainly by EDX detector resolution (see Appendix, Fig. 9).

Figure 2 shows TEM image of a cross section of the heterostructure obtained by JEM-2100 at 200 kV. Elemental analysis was performed by x-ray energy-dispersive system (Oxford Instruments, INCA Energy). The cross-section slice plate for TEM was prepared by FIB using Carl Zeiss Cross Beam Neon 40 EB scanning electron-ion microscope, equipped with an autoemission electron and a gallium ion gun with a resolution of 1 nm. The unit was equipped with a micromanipulator. To protect the sample from damage a 100-nm-thick layer of Pt metal mask was deposited by dc sputtering and then additionally covered by 2- μm -thick Pt film, formed on the sample surface by the gas-injection system for local precursor deposition. Ga⁺ ions with energy of 30 keV were used to obtain the slice and its thinning (polishing) with a gradual decrease of etching current from 5 nA to 5 pA. At the final stage the ion energy was decreased down to 5 keV to remove the broken at 30-keV layer. In the obtained image we clearly observe a sharp enough interface between the LSMO layer and NGO substrate, as well as between the SIO and LSMO layers. The right side of Fig. 2 shows Fourier images from NGO substrate and from SIO and LSMO layers in heterostructure. The coincidence of reflections in Fourier image of the layers SIO/LSMO heterostructure indicates the matching of the crystal lattices and confirms the epitaxial growth of SIO on LSMO. The reflexes of the heterostructure also lie on the part of the reflexes from the substrate (211)LSMO|| (204)NGO and (110)LSMO|| (112)NGO, which is also in agreement with the assumption of epitaxial growth of the heterostructure on the substrate by the proposed cube-on-cube mechanism [38]. The yellow lines are drawn by using electron diffraction data, figure contrast, and energy-dispersive spectroscopy (EDX). A detailed analysis of EDX data gives transition-layer thickness 2–3 nm (see Appendix, Fig. 9), determined mainly by EDX detector size. The estimation of material content by means of EDX across the

interfaces (Fig. 9) shows that there is no intermixing of Ir, Mn, and Nd at the interface on the nanometer scale. The EDX measurement along the cross section also indicated the absence of additional displacement of La and Sr within the experimental uncertainty.

III. SPIN CURRENT

In SIO/LSMO heterostructures the paramagnetic material SIO with a pronounced SOI was used as a normal metal, while the ferromagnetic LSMO is a magnetic half metal. We measured the temperature dependence of resistance and FMR for both LSMO and SIO films [38]. No FMR response was observed at room temperature for SIO film, which demonstrates slow reduction of resistance with lowering T down to $T \approx 100$ K. On other hand, the resistance of reference LSMO film with optimal content of La and Sr (Curie temperature 350 K) demonstrated well-pronounced decrease with the temperature decrease.

The sample has shape of a strip formed on the NGO substrate with metallic (Pt or Au) contacts at the edges. The magnetic properties of the heterostructure and the films were determined either for the case when sample was placed in the rectangular microwave cavity operating at TE_{012} resonant mode at frequency $F = 9.6$ GHz [38], or installed in a microstrip line operating at broad $F = 2\text{--}20\text{--GHz}$ frequency band [40]. The dc controlled external magnetic field was applied in the plane of substrate (110)NGO, while the magnetic component of the microwave field was directed along the normal to the substrate [38]. In order to determine the magnetic anisotropy of the heterostructure, the angular dependencies of FMR spectra were recorded and allowed to obtain the resonance field H_0 as a function of the magnitude of the equilibrium magnetization M and anisotropy fields $H_u = 2K_u/M$ and $H_c = 2K_c/M$, where K_u and K_c are the uniaxial and the biaxial cubic anisotropy constants, correspondingly. At room temperature only the FMR spectral lines from the LSMO layer were observed, since the sensitivity of the spectrometer does not allow recording the absorption spectrum from paramagnetic SIO layer [38]. Also, we did not observe any significant deviation of M for LSMO film after deposition of SIO on top. Some variations of H_u and H_c in SIO/LSMO heterostructure were observed. Characteristics of the normalized magnetization of LSMO and SIO/LSMO, measured using the magneto-optical Kerr effect, are presented in the Appendix, Fig. 12, indicating that a difference for LSMO film and SIO/LSMO heterostructure in saturation H_S and coercive H_C fields does not exceed 40 and 15%, correspondingly.

The spin current j_S was generated under the FMR pumping while the external field H was swept across the resonance field H_0 . The recording voltage V taken from the contacts on strip contain the voltage component V_Q induced by spin current flow caused by FMR. The output dependences $V(H)$ were obtained using data accumulation technique. The typical signals $V(H)$ from SIO/LSMO heterostructure are shown in Fig. 3 for two frequencies, $F = 2.6$ GHz and $F = 9.0$ GHz [38,39]. The experimental dependences are the sum of spin voltage component V_Q induced by FMR and the contribution

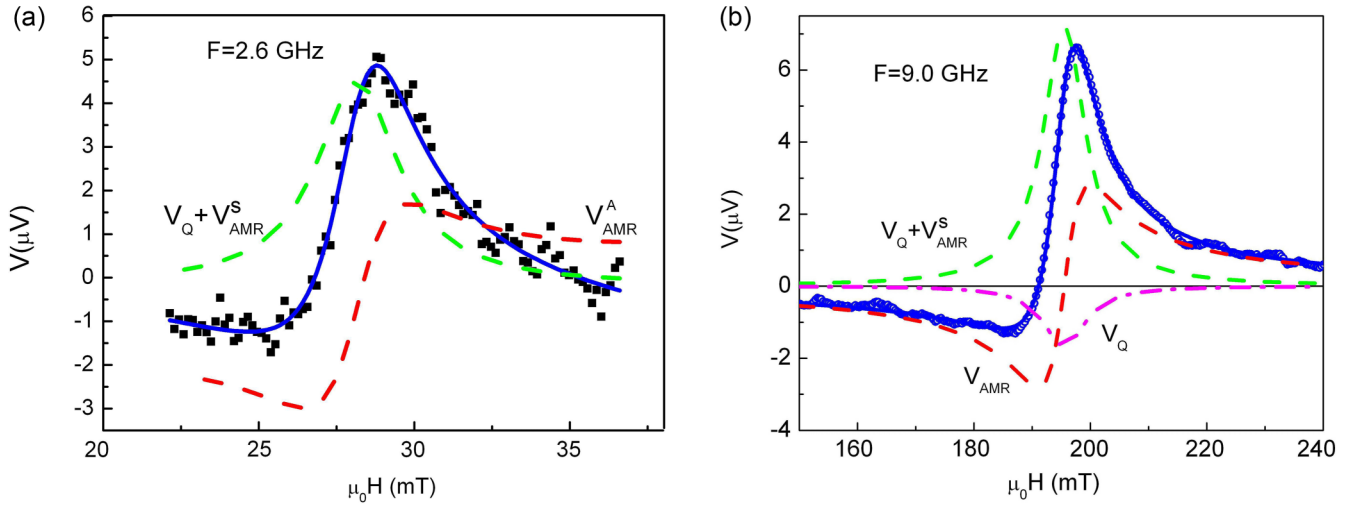


FIG. 3. Spectra of the voltage induced by spin current generation under FMR pumping at frequencies: (a) 2.6 GHz, (b) 9.0 GHz, $T = 300$ K. Experimental data are shown by symbols with fitting functions given by solid blue lines. Dashed lines show contributions of V_Q , V_{AMR}^S , and V_{AMR}^A are marked by the appropriate subscripts.

of anisotropic magnetoresistance (AMR) [16,41]:

$$V = [V_{AMR}^S L(H) + V_{AMR}^A D(H)] \sin 2\phi \sin \phi_0 + V_Q L(H) \cos \phi, \quad (1)$$

where $L(H) = \Delta H^2 / [(H - H_0)^2 + \Delta H^2]$ is the symmetric Lorentz function, $D(H) = \Delta H(H - H_0) / [(H - H_0)^2 + \Delta H^2]$ is the dispersion function, ΔH is the linewidth, V_{AMR}^S and V_{AMR}^A are the amplitudes of symmetric and asymmetric parts of AMR contribution, respectively, $V_Q(H)$ is the ISHE voltage caused by spin current j_s flow through the SIO/LSMO interface, and ϕ is the angle between dc magnetic field and current set across the SIO/LSMO strip. The ratio $V_{AMR}^A / V_{AMR}^S = -tg\phi_l$ [16], where ϕ_l is the phase difference between microwave current and microwave magnetization and it was taken as $\phi_l \approx \pi/4$ in our case [38]. For the case of asymmetric AMR $V_{AMR}^A = 0$ at $\mu_0 H = \mu_0 H_0 = 195.7$ mT [see Fig. 3(b)] we estimated the ratio $V_Q / V_{AMR}^S = 0.3 \pm 0.03$. The experimental value of $V_Q = 1.7$ μ V was obtained at the maximal microwave power of Gunn diode oscillator (around 100 mW) at $F = 9.0$ GHz.

Spin current j_s induced by FMR spin pumping across a N/F interface is determined by the changing of magnetization and the components, proportional to the real ($\text{Re}g^{\uparrow\downarrow}$) and the imaginary ($\text{Im}g^{\uparrow\downarrow}$) parts of spin mixing conductance [6,42,43]:

$$j_s = \frac{\hbar}{4\pi} \left(\text{Re}g^{\uparrow\downarrow} m \frac{dm}{dt} + \text{Im}g^{\uparrow\downarrow} \frac{dm}{dt} \right), \quad (2)$$

where m is normalized magnetization in ferromagnetic F layer. A family of magnetic field dependences of the transmitted microwave coefficient $S_{21}(H)$ recorded under FMR pumping at the fixed frequency within $F = 2\text{--}20$ -GHz band were used for determination of $\text{Re}g^{\uparrow\downarrow}$ and $\text{Im}g^{\uparrow\downarrow}$ (see Fig. 10 and Ref. [44]).

The Gilbert spin damping coefficient α characterizes spin precession attenuation, and a broadening of FMR linewidth ΔH is seen in α increase caused by spin current

generation across the N/F interface [6,21,42,43]. Figure 4(a) shows $\Delta H(F)$ dependences obtained from the measurements of FMR transmitted spectra $S_{21}(H)$ for either LSMO film or SIO/LSMO heterostructure. The Gilbert spin damping α and the linewidth broadening ΔH can be determined using equation [43]

$$\Delta H(F) = 4\pi\alpha F / \gamma + \Delta H_0, \quad (3)$$

where γ is the gyromagnetic ratio and ΔH_0 is the inhomogeneous broadening. Here, we neglect the impact of other sources of spin damping (see, for example, Ref. [45]). For LSMO film we obtain spin damping $\alpha_{\text{LSMO}} = 2.0 \pm 0.2 \times 10^{-4}$, and an increased value of $\alpha_{\text{SIO/LSMO}} = 6.7 \pm 0.8 \times 10^{-4}$ for SIO/LSMO heterostructure after SIO deposition on top of LSMO. The frequency-independent broadening of resonant linewidth ΔH_0 at low frequencies $F < 6$ GHz $\mu_0 \Delta H_0 = 0.6 \pm 0.1$ mT is small and could be attributed to a magnetic inhomogeneity of the heterostructure. At higher frequencies broadening of FMR linewidth and increase of Gilbert damping allows to estimate the real part of spin mixing conductance as follows [6,42,43,46]:

$$\text{Re}g^{\uparrow\downarrow} = \frac{4\pi M d_{\text{LSMO}}}{g\mu_B} (\alpha_{\text{SIO/LSMO}} - \alpha_{\text{LSMO}}), \quad (4)$$

where $M = 370$ kA/m is LSMO film magnetization, $d_{\text{LSMO}} = 30$ nm is LSMO film thickness, $\mu_B = 9.27 \times 10^{-24}$ J/T is the Bohr magneton, Landé factor $g = 2$. From Eq. (4) we got $\text{Re}g^{\uparrow\downarrow} = (3.5 \pm 0.5) \times 10^{18} \text{ m}^{-2}$. Note, $\text{Re}g^{\uparrow\downarrow} = 1.3 \times 10^{18} \text{ m}^{-2}$ was obtained in Ref. [44] for the SIO/LSMO heterostructure fabricated by laser ablation. According to Ref. [35], when the SIO film thickness changes from 1.5 to 12 nm the $\text{Re}g^{\uparrow\downarrow}$ for SIO/LSMO heterostructure changes from $0.5 \times 10^{19} \text{ m}^{-2}$ to $3.6 \times 10^{19} \text{ m}^{-2}$, respectively.

The theory based on the spin-exchange interaction between localized moments and conductivity electrons shows that the deterministic material properties for $\text{Re}g^{\uparrow\downarrow}$ are the electrical resistivity ρ_{SIO} and the spin-diffusion length λ_{SIO} of N metal;

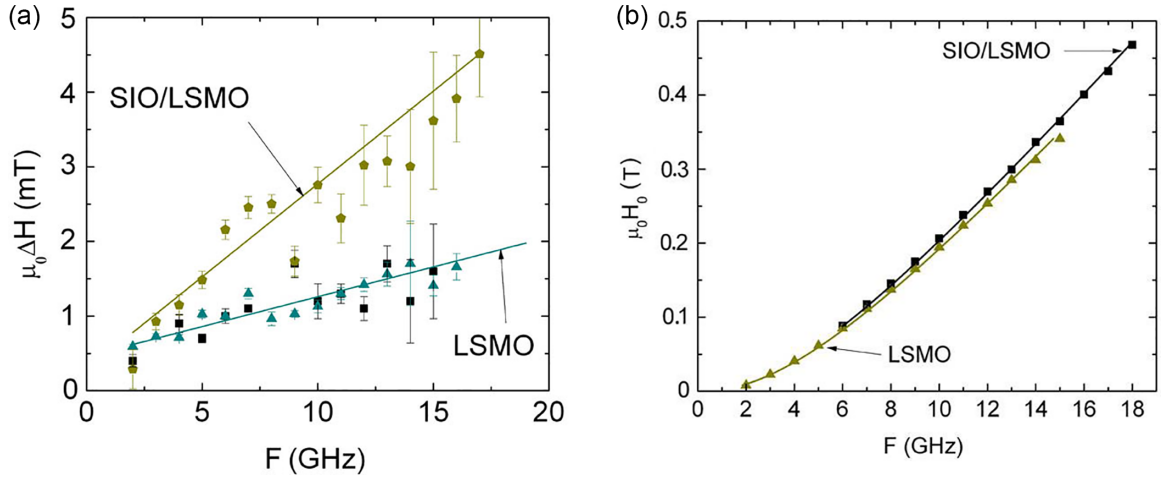


FIG. 4. (a) Frequency dependence of the FMR linewidth ΔH for the LSMO film and the SIO/LSMO heterostructure. Solid lines show linear approximations of the experimental data for $\Delta H(F)$, Eq. (3). (b) Frequency dependence of the resonance field dependence $H_0(F)$ for LSMO film and the SIO/LSMO heterostructure. Symbols are experimental data; solid lines show approximations (6) calculated for fixed $M = 370$ kA/m, $\mu_0 H_u = 1.1$ mT using in gyromagnetic ratio γ for SIO/LSMO heterostructure.

it is SIO film in our case [42,46,47]:

$$\text{Re}g^{\uparrow\downarrow} \approx (h/e^2)/(\rho_{\text{SIO}}\lambda_{\text{SIO}}). \quad (5)$$

Taking $h/e^2 \approx 25.8$ k Ω from Eq. (5), which is valid for a transparent interface and represents the lowest limit of $\text{Re}g^{\uparrow\downarrow}$, for $\lambda_{\text{SIO}} = 1$ nm [36] and $\rho_{\text{SIO}} = 3 \times 10^{-4}$ Ω cm [38] we got $\text{Re}g^{\uparrow\downarrow} \approx 8.6 \times 10^{18}$ m $^{-2}$. The estimation roughly agrees with the experimental data for several 3d transition metals [48]. There are several ferromagnetics investigated in Ref. [48]. Among ferromagnetics in Ref. [48], data for metallic ferromagnetic Co, Ni, Fe, and P are presenting. The average real part of spin mixing conductivity $\text{Re}g^{\uparrow\downarrow}$ for all used ferromagnetic layers is in the range 6×10^{18} – 8×10^{20} m $^{-2}$. Nevertheless, Eq. (5) gives just a qualitative insight for impact of material parameters on $\text{Re}g^{\uparrow\downarrow}$ and does not take into account the influence of SOI on interface properties of the heterostructure. Note the used ρ_{SIO} well correspond to the data 5×10^{-3} Ω cm in Ref. [38].

Figure 4(b) shows the dependences $H_0(F)$ for a LSMO film and SIO/LSMO heterostructure when dc magnetic field was directed along the easy magnetization axis. Using experimental data of $H_0(F)$ we determined the fitting curves using values of magnetization M , uniaxial magnetic anisotropy H_u and variation of γ by the Kittel relation:

$$F = \gamma(4\pi M + H_u + H_0)^{1/2}(H_0 + H_u)^{1/2}. \quad (6)$$

At high frequencies, $F > 10$ GHz, a deviation of the $H_0(F)$ dependence for SIO/LSMO heterostructures from the LSMO film one is clearly observed [Fig. 4(b)]. The observed deviation using the approach in Ref. [42] can be fitted by a recalculated $H_0(f)$ function in terms of deviation in gyromagnetic ratio γ , which could be caused by presence of the imaginary component $\text{Im}g^{\uparrow\downarrow}$ in the case of SIO/LSMO heterostructure. The relative change $\delta\gamma/\gamma_0 = 0.036 \pm 0.001$ caused by sputtering SIO on top of LSMO gives a fitting curve

in Fig. 4(b) and allows to determine $\text{Im}g^{\uparrow\downarrow}$ [6,42,46]:

$$\delta\gamma/\gamma_0 = \text{Im}g^{\uparrow\downarrow} \frac{g_0\mu}{4\pi M d_{\text{LSMO}}}. \quad (7)$$

For the heterostructure shown in Fig. 4(b) we obtain $(\text{Im}g^{\uparrow\downarrow})_{\text{max}} = (46 \pm 1) \times 10^{19}$ m $^{-2}$ for $M = 370$ kA/m, $d_{\text{LSMO}} = 50$ nm [50]. This value noticeably exceeds that obtained earlier for platinum/ferromagnetic structures [6,46,48].

Perhaps the H_u and M variations after SIO deposition on top of LSMO film should be taken into account for estimation of $\text{Im}g^{\uparrow\downarrow}$. For checking this we recall our FMR measurements of angular dependences of LSMO film and SIO/LSMO heterostructures at $F = 9.6$ GHz [38,49]. These measurements showed that the cubic anisotropy H_c is small and can be neglected. A minor decrease of M , less than 2%, and an increase of H_u for approximately twice from LSMO film to SIO/LSMO heterostructure were observed. No FMR response was detected from a single paramagnetic SIO at room temperature.

Figure 11(a) demonstrates the changes of $H_0(F)$ with increasing H_u for FMR studies obtained in wide-frequency band. It can be seen that the theoretical dependences (6) deviate from the experimental data for SIO/LSMO interface with increasing H_u above $\mu_0 H_u = 1.1$ mT. So, the variation of H_u does not explain $H_0(F)$ dependence of SIO/LSMO heterostructure.

On the other hand, decreasing M from 370 to 330 kA/m, relation (6) describes well the data for SIO/LSMO heterostructure [see Fig. 11(b), Appendix]. However, there are no physical grounds for induced ferromagnetism due to proximity effect in SIO with manganites, resulting in changing M after deposition of SIO film on LSMO film. The data in Ref. [51] indicate that magnetic proximity effect is observed at very low temperature in a heterostructure with SIO film on top. In Ref. [49] we also presented the data on appearance of additional ferromagnetism in SIO/LSMO heterostructure at low $T < 50$ K. It was confirmed by an additional ferromagnetic resonance appearing at low T . An appearance of a

thin transition interlayer at SIO/LSMO interface may affect the total resistance of SIO/LSMO heterostructure, but not magnetic properties being of order or thinner than a dead layer in ferromagnetic structures.

The $\delta\gamma/\gamma_0$ lies within the measurement error $\delta\gamma/\gamma_0 \approx 0.001$, giving minimal $(\text{Im}g^{\uparrow\downarrow})_{\min} \approx 10^{19} \text{ m}^{-2}$. As shown in Refs. [38,46,47] for $\text{Im}g^{\uparrow\downarrow}$ comparing with $\text{Re}g^{\uparrow\downarrow}$ the properties of the interface between the ferromagnetic and the normal metal and the quality of the interface may play an important role. The measurements of the spin Hall magnetoresistance for Pt/EuS and W/EuO [52,53] demonstrate an excess in $\text{Im}g^{\uparrow\downarrow}$ over $\text{Re}g^{\uparrow\downarrow}$ by factors 3 and 10, respectively. Note, in addition to a possible change of in-plane magnetization of LSMO an appearance of out-of-plane magnetic moment could also take place as has been observed in manganite/iridate superlattices [29].

IV. SPIN HALL MAGNETORESISTANCE

The measurement of magnetoresistance (MR) is an effective method for probing the spin-related properties in the normal metal layer such as the spin Hall angle and the spin-diffusion length [7–12,52,53]. If the SHE and ISHE processes are coupled by SOI a change in MR becomes spin dependent [3,8]. The relationship of charge-current density \vec{j}_Q induced by ISHE and spin current j_S characterized by spin Hall angle θ_{SH} is determined by the following equation [4,43]:

$$\vec{j}_Q = \theta_{SH} \frac{2e}{\hbar} [\vec{n} \times \vec{j}_S], \quad (8)$$

where \vec{n} is unit vector of spin momentum direction.

The heterostructure SIO/LSMO deposited on NGO substrate was fabricated for measurements in planar Hall configuration with electric contacts at the edges (Fig. 5). Either a voltage V_L , proportional to the longitudinal MR, or a transverse voltage V_T (transverse MR) were measured using a low-noise, frequency-selective lock-in amplifier when current $I = 0.5 \text{ mA}$ at frequency $F \sim 1.1 \text{ kHz}$ was applied along the x direction (see Fig. 5). The MR $R(H)$ was calculated by division of voltage V_L (or V_T) on the current to I . Resistance R_0 at $H = 0$ was used for normalization. External magnetic field H was swept in sequence: $0 \rightarrow H_+ \rightarrow 0 \rightarrow H_- \rightarrow 0$ with a step $\Delta H = H_{\text{MAX}}/N$, $N = 200\text{--}1500$, $H_+ = H_{\text{MAX}}$, $H_- = -H_{\text{MAX}}$. For changing the angle φ between magnetic field H and current I the substrate was rotated around normal to substrate. The direction of the field H is set by the Helmholtz coils.

Comparing the MR for SIO/LSMO heterostructure with a single LSMO film, for which only AMR was *a priori* anticipated, the impact of longitudinal SMR was revealed. The magnetic field dependences for normalized variation of MR $\Delta R/R_0 = (R - R_0)/R_0$ for LSMO and SIO/LSMO are given in Fig. 6, denoted by the subscripts AMR and L , correspondingly.

As seen from Fig. 6(a), for LSMO film the 90° rotation of φ changes the sign of $(\Delta R/R_0)_{\text{AMR}}$ demonstrating a linear rise with H at $0 < H < |H_{\text{MAX}}|$. An oscillating behavior of $\Delta R/R_0$ as $\cos 2\varphi$ between curves (1) and (2) was observed as expected for AMR [9,54]. This is seen also in Fig. 6(b), where H - φ plane is given for LSMO with $\Delta R/R_0$ given by the color

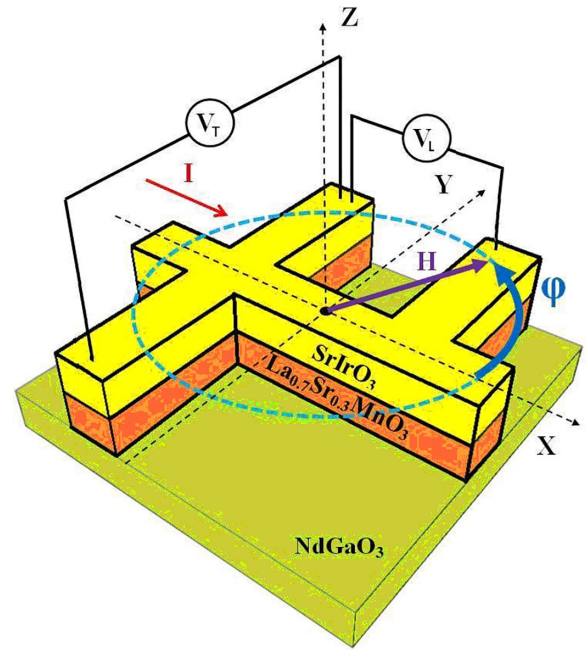


FIG. 5. $\text{SrIrO}_3/\text{La}_{0.7}\text{Sr}_{0.3}\text{MnO}_3$ heterostructure on (110) NdGaO_3 substrate and a four-probe MR measurement scheme used for transverse V_T and longitudinal V_L voltage output terminals. Angle φ between direction of magnetic field H and current I was changed by rotation of substrate in X - Y plane. The width of strip line in heterostructure 100–500 μm ; the distance between contacts 1.5 mm for resistance measurements scheme.

scale. Similar dependencies for SIO/LSMO are presented in Figs. 6(c) and 6(d). In this case the $(\Delta R/R_0)$ vs H lies always below R_0 , being negative.

Figure 7 demonstrates the longitudinal MR $(\Delta R/R_0)_L$ of angular dependences for either LSMO film or SIO/LSMO heterostructure. The first one is associated with the AMR of LSMO film, while the second dependence contains contributions of both the SMR and AMR in the heterostructure. The AMR is observed in metallic ferromagnetics and shows an oscillating dependence of MR on the angle φ between the direction of electric current I and the magnetization. For the case when axis of ferromagnetic material anisotropy coincides with current I direction the relation for the variation of longitudinal MR on the angle is simplified [9,54]:

$$\left(\frac{\Delta R}{R_0}\right)_L = \left(\frac{\Delta R}{2R_0}\right)_{\text{AMR}} \cos 2\varphi, \quad (9)$$

where the angle φ could be counted between current I direction and the in-plane magnetic field H . In Fig. 7 curve (1) shows that the longitudinal $(\Delta R/R_0)_L$ angular dependence for LSMO film fits Eq. (9). Curve (2) in Fig. 7 demonstrates angular variation of MR for SIO/LSMO heterostructure [9,54]. For the both cases experimental data were obtained at the external magnetic field $\mu_0 H = 9 \text{ mT}$.

In normal metals (without magnetic order) electrons with spin-up and spin-down degenerate and AMR is absent. We did not observe AMR response in SIO film at room temperature and cooling down to 100 K. As mentioned earlier, in a bilayer structure with ferromagnetic and nonmagnetic metal,

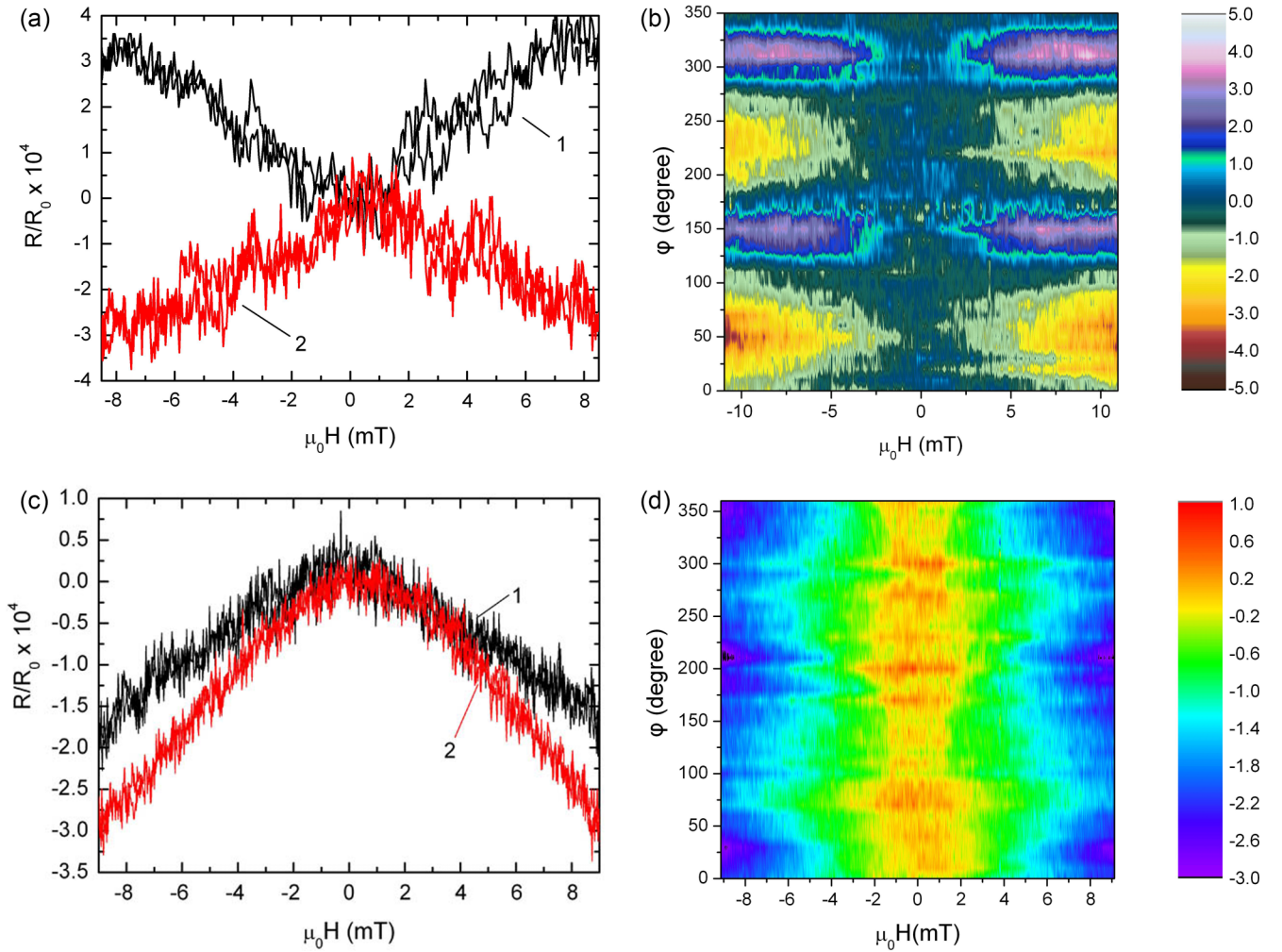


FIG. 6. Variation of MR ($\Delta R/R_0$), normalized on $R_0 = R(H = 0)$. (a) Magnetic field dependence of $(\Delta R/R_0)_{\text{AMR}}$ for LSMO film at two angles $\varphi = 140^\circ$ (1) and $\varphi = 230^\circ$ (2) and (b) H - φ cut of 3D magnetoresistance image for LSMO film; (c) longitudinal $(\Delta R/R_0)_L$ vs H for SIO/LSMO heterostructure at $\varphi = 30^\circ$ (1) and $\varphi = 80^\circ$ (2). (d) H - φ image for SIO/LSMO heterostructure. The $(\Delta R/R_0)$ amplitudes are given in colored scale multiplied by 10^4 (b), (d).

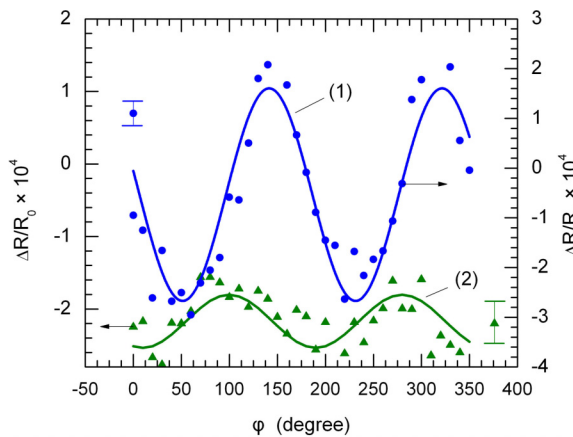


FIG. 7. Angular dependencies of longitudinal MR ($\Delta R/R_0$) for LSMO film (filled circles) and SIO/LSMO heterostructure (triangles) measured at external magnetic field $\mu_0 H = 9$ mT. Fitting dependences Eq. (9) and Eq. (10) are shown by solid lines (1) for LSMO film, (2) for SIO/LSMO heterostructure, correspondingly. Uncertainties are shown by the error bars.

exhibiting strong SOI, the longitudinal MR contains the SMR term. In such structures a charge current generates pure spin current [7,55,56] with an efficiency characterized by spin Hall angle θ_{SH} . For SIO/LSMO heterostructure the longitudinal MR takes the form containing both SMR and AMR components [9,54]:

$$\left(\frac{\Delta R}{R_0}\right)_L = \left(\frac{\Delta R}{R_0}\right)_0 + \left(\frac{\Delta R}{2R_0}\right)_1 [1 + \cos 2\varphi], \quad (10)$$

where

$$\left(\frac{\Delta R}{R_0}\right)_0 = -\theta_{SH}^2 \frac{2\lambda_{\text{SIO}}}{d_{\text{SIO}}}, \quad (11)$$

$$\left(\frac{\Delta R}{R_0}\right)_1 = \theta_{SH}^2 \frac{\lambda_{\text{SIO}}}{d_{\text{SIO}}} \text{Re} \frac{2\lambda_{\text{SIO}}\rho_{\text{SIO}}(\text{Re}G^{\uparrow\downarrow} + i\text{Im}G^{\uparrow\downarrow})}{1 + 2\lambda_{\text{SIO}}\rho_{\text{SIO}}(\text{Re}G^{\uparrow\downarrow} + i\text{Im}G^{\uparrow\downarrow})}. \quad (12)$$

The presence of (11) term could shift MR to the negative value [see Figs. 6(a) and 6(c)]. In (12) the presence of a imaginary part of spin mixing conductance

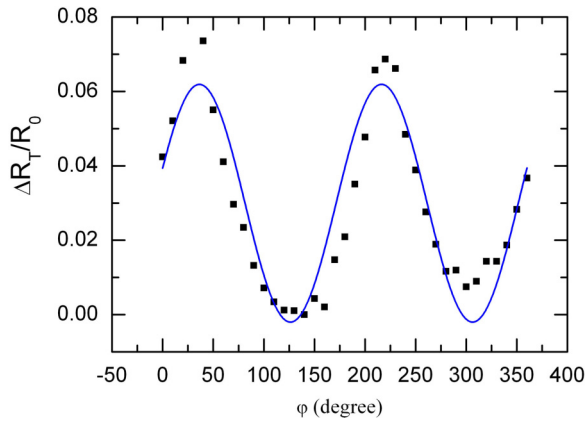


FIG. 8. Angular dependencies of variation of transverse MR ($\Delta R/R_0$) for SIO/LSMO heterostructure (filled squares) measured at $\mu_0 H = 9$ mT. Fitting dependence $\sim \sin 2\varphi$ function is shown by the solid line.

$\text{Im}G^{\uparrow\downarrow}$ is considered as well. Taking resistivity of the SIO film $\rho_{\text{SIO}} = 3 \times 10^{-4} \Omega \text{ cm}$ [38] and parameters obtained in part 3: $\text{Re}G^{\uparrow\downarrow} = \text{Re}\rho^{\uparrow\downarrow} e^2/h = 1.35 \times 10^{10} \text{ cm}^{-2} \Omega^{-1}$ and $\text{Im}G^{\uparrow\downarrow} = \text{Im}\rho^{\uparrow\downarrow} e^2/h = 3.9 \times 10^{10} \text{ cm}^{-2} \Omega^{-1}$, $2\lambda_{\text{SIO}}\rho_{\text{SIO}} \text{Re}G^{\uparrow\downarrow} = 0.81$, and $2\lambda_{\text{SIO}}\rho_{\text{SIO}} \text{Im}G^{\uparrow\downarrow} = 2.33$. For $\lambda_{\text{SIO}} = 1$ nm [36] and $d_{\text{SIO}} = 10$ nm and $(\Delta R/R_0)_0 = -(2.2 \pm 0.05) \times 10^{-4}$ (see Fig. 7, curve 2) we got from Eq. (11) $\theta_{SH} = 0.033 \pm 0.005$. The estimation of θ_{SH} in this case should take into account the part independent of φ in Eq. (10), which is 3 times less $(\Delta R/R_0)_1 = (0.7 \pm 0.14) \times 10^{-4}$. So, negative value of $(\Delta R/R_0)$ could be caused by $(\Delta R/R_0)_0$ from Eq. (11). From Eq. (12) we obtain $\theta_{SH} = 0.03 \pm 0.01$ if we take into account the components dependent on angle φ . Since we do not fix the absolute value of the magnetoresistance, then the last estimation is more correct.

In calculation of SMR the data were taken from measurements at magnetic fields smaller than the saturation field H_S (see Appendix, Fig. 12). As can be seen from Appendix, Fig. 12 for LSMO film and SIO/LSMO heterostructure a difference of saturation fields H_S for both samples does not exceed 40%. The calculated SMR value increases with $(\Delta R/R_0)$ almost linearly with the magnetic field up to $H = H_S$ and then at $H \gg H_S$ saturates where the Hanle effect takes place [57].

The decrease of measured SMR in the SIO/LSMO heterostructure is the shunting of the LSMO and SIO films resistances by a conductive layer at the SIO/LSMO interface [38]. In this case the resistance (R_H^1) of the SIO/LSMO heterostructure can be modeled as a parallel connection of resistance of the upper layer of SIO film R_S and resistance of the bottom LSMO layer R_L . $R_H^1 = R_S R_L / (R_S + R_L)$ and resulted in a reduced value of measured resistance of heterostructure (R_H) which becomes smaller than the calculated R_H^1 [38]. In experimental conditions it is needed to account also a parallel connection of an additional interface resistance R_I . Using sheet resistance of interface SIO/LSMO $R_I = \rho_I / d_S$ we get $\rho_I = 8 \times 10^{-6} \Omega \text{ cm}$ at low temperature supposing the thickness of interface is of order of 1 nm [38]. A small resistivity of the interface may indicate an existence of a thin, well-conducting layer possibly as observed at the

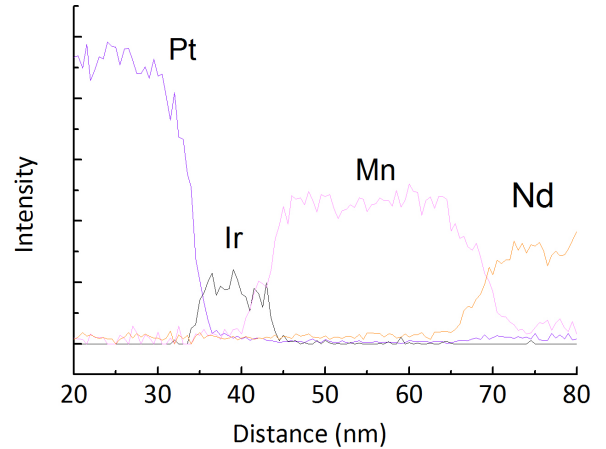


FIG. 9. EDX spectrum for heterostructure covered with Pt. Distance starts approximately 30 nm from the top of SIO layer.

oxide interfaces [56,58,59]. As we can see from Fig. 3 in Ref. [38], the interface resistance increases with T weakly, but it is still lies within the range of order of the same value, lower than the specific resistance of either the LSMO, or SIO films.

The model [60] for iridate/manganite interface shows that charge transfer at the interface from the half-filled spin-orbit entangled $J_{\text{eff}} = 1/2$ state to the empty $e^{\uparrow g}$ states may occur. The charge leakage from the iridate side makes the interface hole doped, while the manganite side of interface in SIO/LSMO heterostructure becomes electron doped. The doped carriers make both sides metallic conducting. Chemically, the La and Sr doping across the interface, or oxygen doping that may affect the interface conductivity, are not excluded [29,61]. The measurements of cross-section elemental content (see Appendix, Fig. 9) using EDX show there is no overmixing of La and Sr elements at interface within the experimental uncertainty. Nonchemically abrupt interfaces could happen, not only in iridate/manganite interface [62]. Recently we observed the variation of resistance for interface

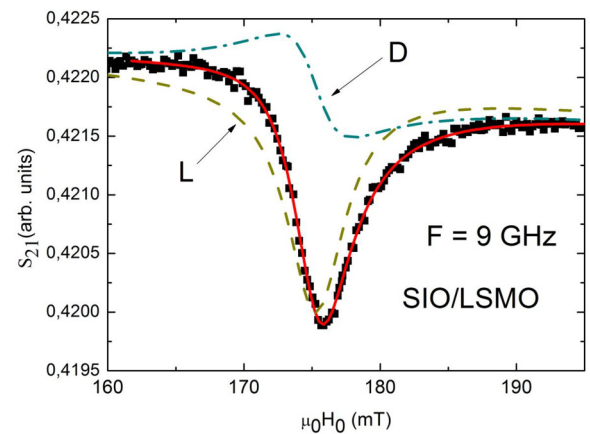


FIG. 10. Magnetic field dependence $S_{21}(H)$ for SIO/LSMO heterostructure under microwave radiation at $F = 9$ GHz in microstrip configuration. Solid line shows the approximation of the spectrum, L is Lorentz line, and D is dispersion relation.

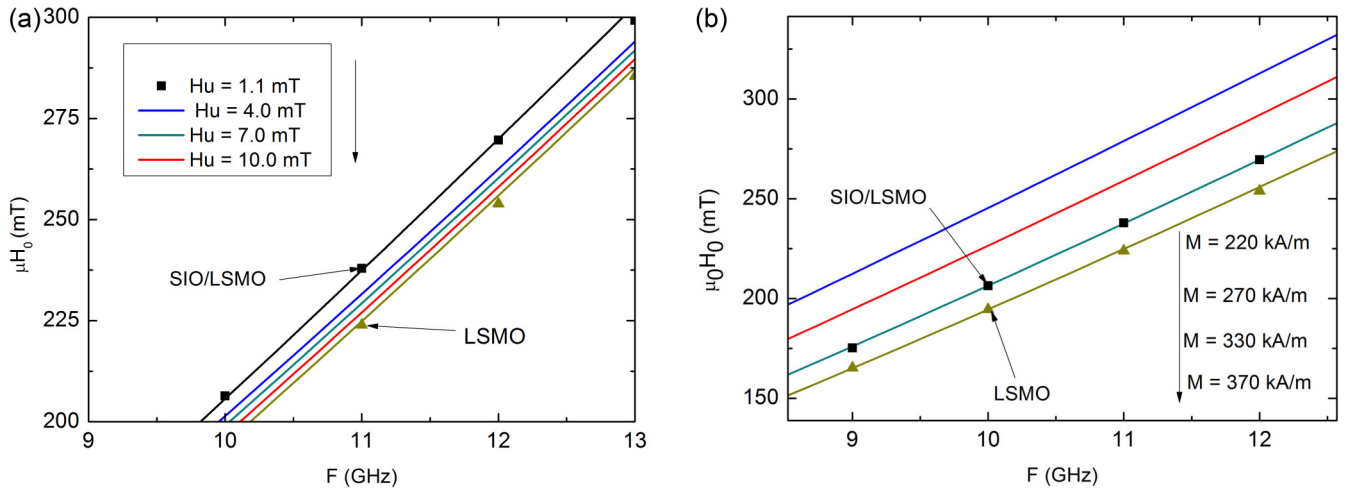


FIG. 11. (a) Calculated by Eq. (6) $H_0(F)$ dependences for $\mu_0 H_u = 1.1, 4.0, 7.0,$ and 10.0 mT with fixed $M = 370$ kA/m. Curves are arranged from top to bottom with increase of H_u . Squares and triangles denote experimental values for SIO/LSMO and LSMO, respectively. (b) $H_0(F)$ for fixed $\mu_0 H_u = 1.1$ mT and four values of $M = 220, 270, 330,$ and 370 kA/m (see arrow from top to bottom); squares and triangles denote the experimental values for SIO/LSMO and LSMO, respectively.

layer changing the sequence of layer material deposition (see Ref. [38]). In general, it is interesting to insert an additional layer in between LSMO and SIO as was done in Ref. [63] where NbN metallic spacer covers on NiFe remained transparent for spin current. It may give another physical picture in that case. However, any additional spacer will result in two new interfaces with a complicated behavior.

In our measurements configuration (see Fig. 5) with applied dc current I along the x direction, for the voltage taken along the y direction we get the variation of the transverse MR, which is usually referred to also as a planar Hall effect magnetoresistance [9,54]:

$$\left(\frac{\Delta R}{R}\right)_T = \left(\frac{\Delta R}{2R}\right)_1 \sin 2\varphi + \left(\frac{\Delta R}{R}\right)_2 \cos \theta, \quad (13)$$

where θ is the angle for out-of-plane magnetization along z (not shown in Fig. 5) relative to the direction of the current I . The measured transverse MR value gives $(\Delta R/R)_1 = 0.032 \pm 0.002$ and, considering that in planar Hall effect configuration the conductive layer at the interface SIO/LSMO has no influence, $\rho_I \ll \rho_H^1$, does not shunt SMR. Using Eq. (13) we get $\theta_{SH} = 0.65 \pm 0.05$. Finally, from transverse SMR (see Fig. 8) we obtained θ_{SH} about 20 times larger than from longitudinal MR. Note, the second term in Eq. (13) may arise from the magnetization directed perpendicular to the plane [60], determined by the angle θ between the magnetization and the substrate plane. Recently, spin Hall angle $\theta_{SH} = 0.76$ in Py/SrIrO₃ heterostructure [30] was reported and $\theta_{SH} = 1.1$ at room temperature for SrIrO₃/Co_{1-x}Tb_x [32]. So, heterostructures with the strontium iridate show remarkably large

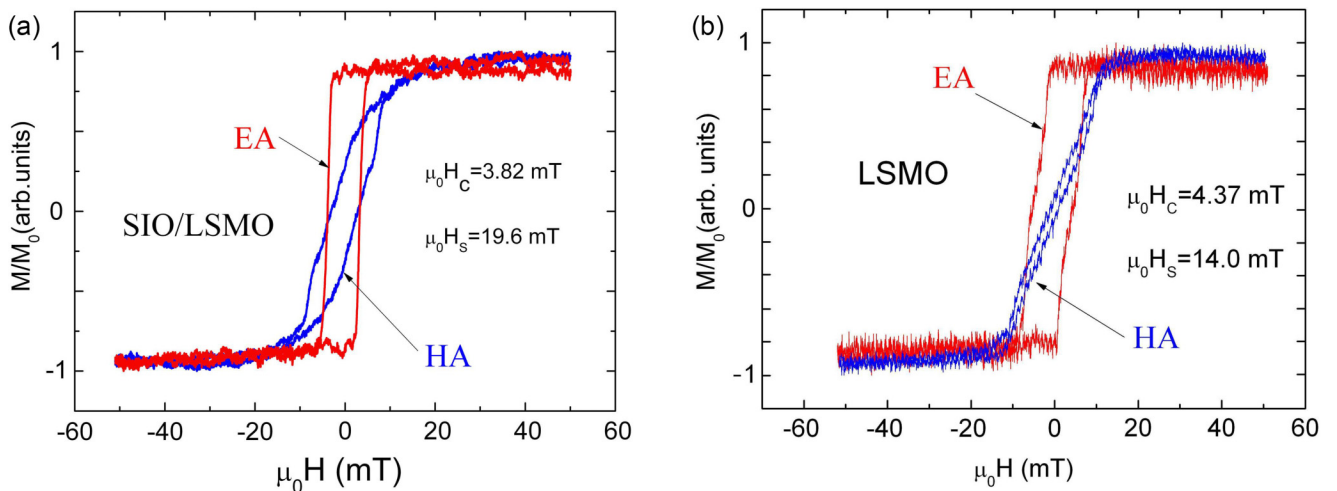


FIG. 12. Magnetic field dependence of the normalized magnetization of the SIO/LSMO heterostructure (a) and LSMO film (b), measured using the Kerr magneto-optical effect. Dependences marked by EA (red line) and HA (blue line) correspond to easy axis and hard axis, correspondingly. Coercive force H_C and saturation field H_S are given in the figures.

values of θ_{SH} , significantly larger than the value of $5d$ transition metals, being comparable to those reported for systems with topological materials [48].

V. CONCLUSIONS

The transmission electron microscope investigation and x-ray diffraction measurements of $\text{SrIrO}_3/\text{La}_{0.7}\text{Sr}_{0.3}\text{MnO}_3$ heterostructure show epitaxial growth by cube on cube of both films in the heterostructure with a smooth interface. It was shown that in regime of ferromagnetic resonance the voltage response induced by anisotropic magnetoresistance is roughly twice larger than the response induced by generation of spin current flowing across the interface. The real and imaginary parts of spin mixing conductance of heterostructure were determined from frequency dependence of ferromagnetic resonance magnetic field. Obtained data for the real part of spin mixing conductance agrees with the experimental data obtained previously and give a realistic qualitative insight into impact of material parameters used in experiment. The imaginary part of spin mixing conductance of $\text{SrIrO}_3/\text{La}_{0.7}\text{Sr}_{0.3}\text{MnO}_3$ interface was found extremely high. The spin Hall angle was determined by measuring the spin magnetoresistance, and contribution of anisotropic magnetoresistance on measured data was evaluated for estimation of spin Hall magnetoresistance. The interlayer with high conductivity at the interface of $\text{SrIrO}_3/\text{La}_{0.7}\text{Sr}_{0.3}\text{MnO}_3$ heterostructure shunts the measured resistance in longitudinal mode, but has no decisive influence on measurements of transverse MR. Estimation of spin Hall angle for the interface turns out to be higher than for the case of the interface with Pt film.

ACKNOWLEDGMENTS

The authors are grateful to V. V. Demidov, A. M. Petrzhih, K. L. Stankevich, and T. A. Shaikhulov for their help and discussion of experimental results. This work was carried out within the framework of the state task of the Kotelnikov Institute of Radio Engineering and Electronics Russian Academy of Sciences. The study was carried out using the Unique Science Unit “Cryointegral” (Grant No. USU #352529), which was supported by the Ministry of Science and Higher Education of Russia (Project No. 075-15-2021-667). Structural investigations were carried out using the equipment of the

Center “Material Science and Metallurgy” with the financial support of Ministry of Education and Science of Russian Federation (Agreement No. 075-15-2021-696). The activity by G.A.O. on microwave measurements was partially supported by Russian Science Foundation Project No. 23-49-10006.

APPENDIX

Figure 9 shows the data of energy-dispersive spectroscopy of SIO/LSMO/NGO cross section across the line perpendicular to the interface—the yellow dashed lines (Fig. 2) illustrate positions of layers and allow to estimate their widths. The estimation of material content by means of EDX shows that there is no intermixing of Ir, Mn, and Nd at the interface on the nanometer scale. The measurements of cross-section contrast (Fig. 2) using EDX show there is no migration of La and Sr within the experimental uncertainty. The output data for sharpness were restricted by sensitivity of the used detector. LSMO/NGO and Pt/SIO showed somewhat wider interfaces.

The typical $S_{21}(H)$ spectrum for SIO/LSMO heterostructure is presented in Fig. 10. It is approximated using sum of the Lorentz line (L) for the imaginary part of FMR and the dispersion relation for the real part (D) [42]. From fitting the experimental curves with these two components it is possible to determine the resonance field (H_0) and the width of FMR line (ΔH).

The angular dependences of the resonance field showed that after SIO sputtering on the top of LSMO a change in H_u anisotropy field occurs. Figure 11(a) shows the changes in $H_0(F)$ with increasing H_u . It can be seen that the theoretical dependences strongly deviate from the experiment with increasing $\mu_0 H_u$ from 1.1 to 10 mT. On the other hand, with decreasing M from 370 to 330 kA/m the obtained dependence [Eq. (6)] describes well the data for SIO/LSMO [see Fig. 11(b)].

Figure 12(a) shows magnetic field dependences of the normalized magnetization of the SIO/LSMO heterostructure and LSMO film measured using the Kerr magneto-optical effect. In calculation of SMR, the data were taken from measurements at magnetic fields smaller than the H_S saturation field. As can be seen from Fig. 12(b) for LSMO film and Fig. 12(a) SIO/LSMO heterostructure a difference of H_S fields does not exceed 40%. SMR value increases with $(\Delta R/R_0)$ almost linearly with the magnetic field up to $H = H_S$ and then at $H \gg H_S$ saturates.

-
- [1] S. Zhang, *Phys. Rev. Lett.* **85**, 393 (2000).
 - [2] M. I. Dýákonov and V. I. Perel, *Zh. Eksp. Teor. Fiz. Pis. Red.* **13**, 657 (1971).
 - [3] J. E. Hirsch, *Phys. Rev. Lett.* **83**, 1834 (1999).
 - [4] E. Saitoh, M. Ueda, H. Miyajima, and S. Tatara, *Appl. Phys. Lett.* **88**, 182509 (2006).
 - [5] O. Mosendz, V. Vlaminck, J. E. Pearson, F. Y. Fradin, G. E. W. Bauer, S. D. Bader, and A. Hoffmann, *Phys. Rev. B* **82**, 214403 (2010).
 - [6] Ya. Tserkovnyak, A. Brataas, and G. E. W. Bauer, *Phys. Rev. Lett.* **88**, 117601 (2002).
 - [7] J. Sinova, S. O. Valenzuela, J. Wunderlich, C. H. Back, and T. Jungwirth, *Rev. Mod. Phys.* **87**, 1213 (2015).
 - [8] H. Nakayama, M. Althammer, Y.-T. Chen, K. Uchida, Y. Kajiwara, D. Kikuchi, T. Ohtani, S. Geprägs, M. Opel, S. Takahashi, R. Gross, G. E. W. Bauer, S. T. B. Goennenwein, and E. Saitoh, *Phys. Rev. Lett.* **110**, 206601 (2013).
 - [9] Y.-T. Chen, S. Takahashi, H. Nakayama, M. Althammer, S. T. B. Goennenwein, E. Saitoh, and G. E. W. Bauer, *Phys. Rev. B* **87**, 144411 (2013).
 - [10] S. Cho, S. C. Baek, K.-D. Lee, Y. Jo, and B.-G. Park, *Sci. Rep.* **5**, 14668 (2015).

- [11] J. Kim, P. Sheng, S. Takahashi, S. Mitani, and M. Hayashi, *Phys. Rev. Lett.* **116**, 097201 (2016).
- [12] M. Althammer, S. Meyer, H. Nakayama, M. Schreier, M. Weiler, S. Altmannshofer, H. Huebl, S. Geprägs, M. Opel, R. Gross, D. Meier, C. Klewe, T. Kuschel, J.-M. Schmalhorst, G. Reiss, L. Shen, A. Gupta, Y.-T. Chen, G. E. W. Bauer, E. Saitoh, and S. T. B. Goennenwein, *Phys. Rev. B* **87**, 224401 (2013).
- [13] S. O. Valenzuela and M. Tinkham, *Nature (London)* **442**, 176 (2006).
- [14] T. Kimura, Y. Otani, T. Sato, S. Takahashi, and S. Maekawa, *Phys. Rev. Lett.* **98**, 156601 (2007).
- [15] Y. Kajiwara, K. Harii, S. Takahashi, J. Ohe, K. Uchida, M. Mizuguchi, H. Umezawa, H. Kawai, K. Ando, K. Takanashi, S. Maekawa, and E. Saitoh, *Nature (London)* **464**, 262 (2010).
- [16] A. Azevedo, L. H. Vilela-Leão, R. L. Rodríguez-Suárez, A. F. Lacerda Santos, and S. M. Rezende, *Phys. Rev. B* **83**, 144402 (2011).
- [17] O. Rousseau and M. Viret, *Phys. Rev. B* **85**, 144413 (2012).
- [18] C. W. Sandweg, Y. Kajiwara, K. Ando, E. Saitoh, and B. Hillebrands, *Appl. Phys. Lett.* **97**, 252504 (2010).
- [19] H. Kurebayashi, O. Dzyapko, V. E. Demidov, D. Fang, A. J. Ferguson, and S. O. Demokritov, *Nat. Mater.* **10**, 660 (2011).
- [20] A. V. Chumak, A. A. Serga, M. B. Jungfleisch, R. Neb, D. A. Bozhko, V. S. Tiberkevich, and B. Hillebrands, *Appl. Phys. Lett.* **100**, 082405 (2012).
- [21] T. Nan, S. Emori, C. T. Boone, X. Wang, T. M. Oxholm, J. G. Jones, B. M. Howe, G. J. Brown, and N. X. Sun, *Phys. Rev. B* **91**, 214416 (2015).
- [22] K. Kondou, H. Sukegawa, S. Mitani, K. Tsukagoshi, and S. Kasai, *Appl. Phys. Express* **5**, 073002 (2012).
- [23] E. Dagotto, in *Nanoscale Phase Separation and Colossal Magnetoresistance*, Springer Series in Solid-State Sciences Vol. 136 (Springer, Berlin, 2003).
- [24] G. Cao and P. Schlottmann, *Rep. Prog. Phys.* **81**, 042502 (2018).
- [25] H. Haeni, P. Irvin, W. Chang, R. Uecker, P. Reiche, Y. L. Li, S. Choudhury, W. Tian, M. E. Hawley, B. Craigo, A. K. Tagantsev, X. Q. Pan, S. K. Streiffer, L. Q. Chen, S. W. Kirchoefer, J. Levy, and D. G. Schlom, *Nature (London)* **430**, 758 (2004).
- [26] X.-L. Qi and S.-C. Zhang, *Rev. Mod. Phys.* **83**, 1057 (2011).
- [27] M. König, S. Wiedmann, C. Brune, A. Roth, H. Buhmann, L. W. Molenkamp, X.-L. Qi, and S.-C. Zhang, *Science* **318**, 766 (2007).
- [28] N. P. Armitage, E. J. Mele, and A. Vishwanath, *Rev. Mod. Phys.* **90**, 015001 (2018).
- [29] D. Yi, J. Liu, S. L. Hsu, L. Zhang, Y. Choi, J. W. Kim, Z. Chen, J. D. Clarkson, C. R. Serrao, E. Arenholz, P. J. Ryan, H. Xu, R. J. Birgeneau, and R. Ramesh, *Proc. Nat. Acad. Sci. USA* **113**, 6397 (2016).
- [30] T. Nan, T. J. Anderson, J. Gibbons, K. Hwang, N. Campbell, H. Zhou, Y. Q. Dong, G. Y. Kim, D. F. Shao, T. R. Paudel, N. Reynolds, X. J. Wang, N. X. Sun, E. Y. Tsymbal, S. Y. Choi, M. S. Rzchowski, Y. B. Kim, D. C. Ralph, and C. B. Eom, *Proc. Nat. Acad. Sci. USA* **116**, 16186 (2019).
- [31] A. S. Everhardt, M. DC, X. Huang, S. Sayed, T. A. Gosavi, Y. Tang, C.-C. Lin, S. Manipatruni, I. A. Young, S. Datta, J.-P. Wang, and R. Ramesh, *Phys. Rev. Mater.* **3**, 051201(R) (2019).
- [32] H. Wang, K.-Y. Meng, P. Zhang, J. T. Hou, J. Finley, J. Han, F. Yang, and L. Liu, *Appl. Phys. Lett.* **114**, 232406 (2019).
- [33] A. Vedyayev, N. Ryzhanova, N. Strelkov, T. Andrianov, A. Lobachev, and B. Dieny, *Phys. Rev. Appl.* **10**, 064047 (2018).
- [34] X. Jia, K. Liu, K. Xia, and G. E. W. Bauer, *Europhys. Lett.* **96**, 17005 (2011).
- [35] X. Huang, S. Sayed, J. Mittelstaedt, S. Karimeddiny S. Susarla, L. Caretta, H. Zhang, V. A. Stoica, T. Gosavi, F. Mahfouzi, Q. Sun, P. Ercius, N. Kioussis, S. Salahuddin, D. C. Ralph, and R. Ramesh, *Adv. Mater.* **33**, 2008269 (2021).
- [36] S. Crossley, A. G. Swartz, K. Nishio, Y. Hikita, and H. Y. Hwang, *Phys. Rev. B* **100**, 115163 (2019).
- [37] L. Liu, G. Zhou, X. Shu, C. Li, W. Lin, L. Ren, C. Zhou, T. Zhao, R. Guo, Q. Xie, H. Wang, J. Zhou, P. Yang, S. J. Pennycook, X. Xu, and J. Chen, *Phys. Rev. B* **105**, 144419 (2022).
- [38] G. A. Ovsyannikov, T. A. Shaikhulov, K. L. Stankevich, Y. Khaydukov, and N. V. Andreev, *Phys. Rev. B* **102**, 144401 (2020).
- [39] T. A. Shaikhulov, V. V. Demidov, K. L. Stankevich, and G. A. Ovsyannikov, *J. Phys. Conf. Ser.* **1389**, 012079 (2019).
- [40] G. A. Ovsyannikov, K. Y. Constantinian, K. L. Stankevich, T. A. Shaikhulov, and A. A. Klimov, *J. Phys. D: Appl. Phys.* **54**, 365002 (2021).
- [41] V. A. Atsarkin, I. V. Borisenko, V. V. Demidov, and T. A. Shaikhulov, *J. Phys. D: Appl. Phys.* **51**, 245002 (2018).
- [42] M. Zwierzycki, Y. Tserkovnyak, P. J. Kelly, A. Brataas, and G. E. W. Bauer, *Phys. Rev. B* **71**, 064420 (2005).
- [43] F. Yang and P. C. Hammel, *J. Phys. D: Appl. Phys.* **51**, 253001 (2018).
- [44] M. Harder, Z. X. Cao, Y. S. Gui, X. L. Fan, and C.-M. Hu, *Phys. Rev. B* **84**, 054423 (2011).
- [45] T. A. Shaikhulov and G. A. Ovsyannikov, *Phys. Solid State* **60**, 2231 (2018).
- [46] J. Dubowik, P. Graczyk, A. Krysztofik, H. Głowinski, E. Coy, K. Załęski, and I. Goscińska, *Phys. Rev. Appl.* **13**, 054011 (2020).
- [47] G. Tatara and S. Mizukami, *Phys. Rev. B* **96**, 064423 (2017).
- [48] F. D. Czeschka, L. Dreher, M. S. Brandt, M. Althammer, M. Weiler, I.-M. Imort, G. Reiss, A. Thomas, W. Schoch, W. Limmer, H. Huebl, R. Gross, and S. T. B. Goennenwein, *Phys. Rev. Lett.* **107**, 046601 (2011).
- [49] V. V. Demidov, N. V. Andreev, T. A. Shaikhulov, and G. A. Ovsyannikov, *J. Magn. Magn. Mater.* **497**, 165979 (2020).
- [50] G. A. Ovsyannikov, K. Y. Constantinian, E. A. Kalachev, and A. A. Klimov, *Tech. Phys. Lett.* **48**, 75 (2022).
- [51] A. Kumar Jaiswal, D. Wang, V. Wollersen, R. Schneider, M. Le Tacon, and D. Fuchs, *Adv. Mater.* **34**, 2109163 (2022).
- [52] J. M. Gomez-Perez, X.-P. Zhang, F. Calavalle, M. Ilyn, C. González-Orellana, M. Gobbi, C. Rogero, A. Chuvilin, V. N. Golovach, L. E. Hueso, F. S. Bergeret, and F. Casanova, *Nano Lett.* **20**, 6815 (2020).
- [53] P. Rosenberger, M. Opel, S. Geprägs, H. Huebl, R. Gross, M. Müller, and M. Althammer, *Appl. Phys. Lett.* **118**, 192401 (2021).
- [54] Y.-T. Chen, S. Takahashi, H. Nakayama, M. Althammer, S. T. B. Goennenwein, E. Saitoh, and G. E. W. Bauer, *J. Phys. Condens. Matter* **28**, 103004 (2016).

- [55] T. Jungwirth, J. Wunderlich, and K. Olejnik, *Nat. Mater.* **11**, 382 (2012).
- [56] C. T. Boone, J. M. Shaw, H. T. Nembach, and T. J. Silva, *J. Appl. Phys.* **117**, 223910 (2015).
- [57] H. Nakayama, Y. Kanno, H. An, T. Tashiro, S. Haku, A. Nomura, and K. Ando, *Phys. Rev. Lett.* **117**, 116602 (2016).
- [58] Y. Tokura, *Phys. Today* **56**(7), 50 (2003).
- [59] S. Thiel, G. Hammer, A. Schmehl, and C. W. Schneider, *J. Mannhart. Sci.* **313**, 1942 (2006).
- [60] S. Bhowal and S. Satpathy, *Phys. Rev. B* **99**, 245145 (2019).
- [61] D. Yi, C. L. Flint, P. P. Balakrishnan, K. Mahalingam, B. Urwin, A. Vailionis, A. T. N'Diaye, P. Shafer, E. Arenholz, Y. Choi, K. H. Stone, J.-H. Chu, B. M. Howe, J. Liu, I. R. Fisher, and Y. Suzuki, *Phys. Rev. Lett.* **119**, 077201 (2017).
- [62] J. Fontcuberta, H. B. Vasili, J. Gàzquez, and F. Casanova, *Adv. Mater. Interfaces* **6**, 1900475 (2019).
- [63] T. S. Suraj, M. Müller, S. Gelder, S. Geprägs, M. Opel, M. Weiler, K. Sethupathi, H. Huebl, R. Gross, M. S. Ramachandra Rao, and M. Althammer, *J. Appl. Phys.* **128**, 083903 (2020).